Rate of Change of Large-Scale Solar-Wind Structure

Mathew J. Owens[1] · Nachiketa Chakraborty[1] · Harriet Turner[1] · Matthew Lang[1] ·
Pete Riley[2] · Mike Lockwood[1] · Luke A. Barnard[1] · Yutian Chi[3]

Abstract

Quantifying the rate at which the large-scale solar-wind structure evolves is important for both understanding the physical processes occurring in the corona and for space-weather forecast improvement. Models of the global corona and heliosphere typically assume that the ambient solar-wind structure is steady and corotates with the Sun, which is generally expected to be more valid at solar minimum than solar maximum, but this has not been well tested. Similarly, assimilation of solar-wind observations into models requires quantitative knowledge of how the reliability of the observations changes with age. In this study we examine 25 years of near-Earth in situ solar-wind observations and 45 years of observation-constrained solar-wind simulations to determine how much the 1-AU solar-wind speed, V, and radial magnetic-field component, B_R, vary between consecutive Carrington rotations (CRs). For the in situ spacecraft observations, we find the rate of change of V and B_R is similar during solar maximum and minimum, particularly when transient interplanetary coronal mass ejections are removed from the data. This is somewhat counter to expectations. Conversely, the rate of change in V and B_R obtained from global heliospheric simulations is strongly correlated with the solar cycle, with the corona and heliosphere being more variable at solar maximum, as expected. Limiting the analysis of the simulations to the solar equatorial region, however, strongly reduces the difference between solar maximum and minimum, bringing the result into close agreement with the in situ observations. This latitudinal sensitivity is explained in terms of the global solar-wind structure over the solar cycle. For the purposes of assimilating in-ecliptic solar-wind observations, we suggest the uncertainty in V should increase by around 3 km s^{-1} per day since the observation was made and 0.1 nT per day for B_R. For observations made at higher latitude, the effect of observation age will be solar-cycle dependent.

Keywords Solar wind · Solar wind, disturbances · Solar cycle · Magnetosphere, geomagnetic disturbances · Coronal mass ejections

✉ M.J. Owens
   m.j.owens@reading.ac.uk

1 Department of Meteorology, University of Reading, Earley Gate, PO Box 243, Reading RG6 6BB, UK

2 Predictive Science Inc., 9990 Mesa Rim Rd., Suite 170, San Diego, CA 92121, USA

3 CAS Key Laboratory of Geospace Environment, Department of Geophysics and Planetary Sciences, University of Science and Technology of China, Hefei, People's Republic of China

                                                                                    ⚛ Springer

1. Introduction

The solar wind propagates almost radially throughout the heliosphere, meaning the large-scale structure of the solar wind at 1 AU is determined primarily by conditions in the upper corona (see Owens, 2020, and references therein, for a recent overview). In the heliosphere, solar rotation can introduce fast and slow solar-wind streams along the same radial line, leading to the formation of compression and rarefaction regions (Pizzo, 1978). If the coronal structure is stable on time scales comparable to the solar-rotation period, these stream-interaction regions (SIRs) will corotate with the Sun (Wilcox and Ness, 1965; Breen et al., 1998).

Transient structures resulting from coronal mass ejections (CMEs, e.g. Webb and Howard, 2012) propagate through the 'ambient' solar-wind structures. While interplanetary CMEs (ICMEs) are responsible for the most severe space weather (Gosling, 1993; Richardson, Cane, and Cliver, 2002), correctly forecasting the ambient solar-wind structure is of space-weather importance for three reasons. Firstly, the ambient solar wind, particularly SIRs, can be geoeffective in its own right (e.g. Richardson, Cane, and Cliver, 2002; Kilpua et al., 2017). Secondly, the ambient solar wind can modulate both the arrival time and properties of ICMEs in near-Earth space (Vrsnak and Gopalswamy, 2002; Cargill, 2004; Case et al., 2008). Thirdly, the ambient solar-wind structure is important for magnetic connectivity between the Sun and Earth, which determines the transport of solar energetic particles (Luhmann et al., 2010; Chollet and Giacalone, 2011).

The magnetic and solar-wind flow structure of the global corona cannot be observed directly, at least not on a routine basis (Antonucci et al., 2020). Instead, the coronal magnetic field (and hence solar-wind flow) can be extrapolated from the observed photospheric field, subject to a number of limitations and approximations (Mackay and Yeates, 2012). Crucially, only the photospheric field on the Earth-pointing face of the Sun can currently be measured, so observations must be accumulated over a full solar rotation (approximately 27.27 days from Earth's view) to give complete longitudinal coverage (e.g. Hoeksema and Scherrer, 1986). Partly for this reason, coronal models are primarily used in the steady-state approximation, particularly in operational space-weather forecasting. The widely used potential-field source-surface (PFSS. Altschuler and Newkirk, 1969; Schatten, Wilcox, and Ness, 1969; Arge et al., 2003) model is intrinsically steady state, whilst time-dependent magnetohydrodyanmic (MHD) approaches (e.g. Linker et al., 1999; Toth et al., 2005; De-Vore and Antiochos, 2008; Yalim, Pogorelov, and Liu, 2017) are run until a steady-sate equilibrium is reached (e.g. Riley et al., 2006). These coronal solutions are then used to drive heliospheric models out to Earth orbit (Riley, Linker, and Mikic, 2001; Odstrcil, 2003; Merkin et al., 2016; Narechania et al., 2021). Methods to produce physically consistent photospheric magnetic-field conditions for the unobserved side of the Sun have been developed (Hickmann et al., 2015), which potentially allow relaxation of the steady-state approximation. However, these time-evolving photospheric fields are still primarily used as 'snapshots' with steady-state coronal models. There are on-going efforts to move towards fully dynamic coronal reconstructions, though these are not yet in routine operational forecasting use (Yeates and Mackay, 2009; Yeates et al., 2010). Given the prevalence of steady-state coronal – and hence steady-state solar-wind – models and forecasts, it is useful to quantify the validity of this approximation and how that changes over the solar cycle.

The general expectation is that the corona evolves more rapidly at solar maximum than minimum. Figure 1 shows examples of white-light images of the solar corona from the Large-angle Spectroscopic Coronagraph (LASCO) instrument on board the Solar and Helio-spheric Observatory (SOHO) spacecraft (Brueckner et al., 1995). Panel b shows the corona
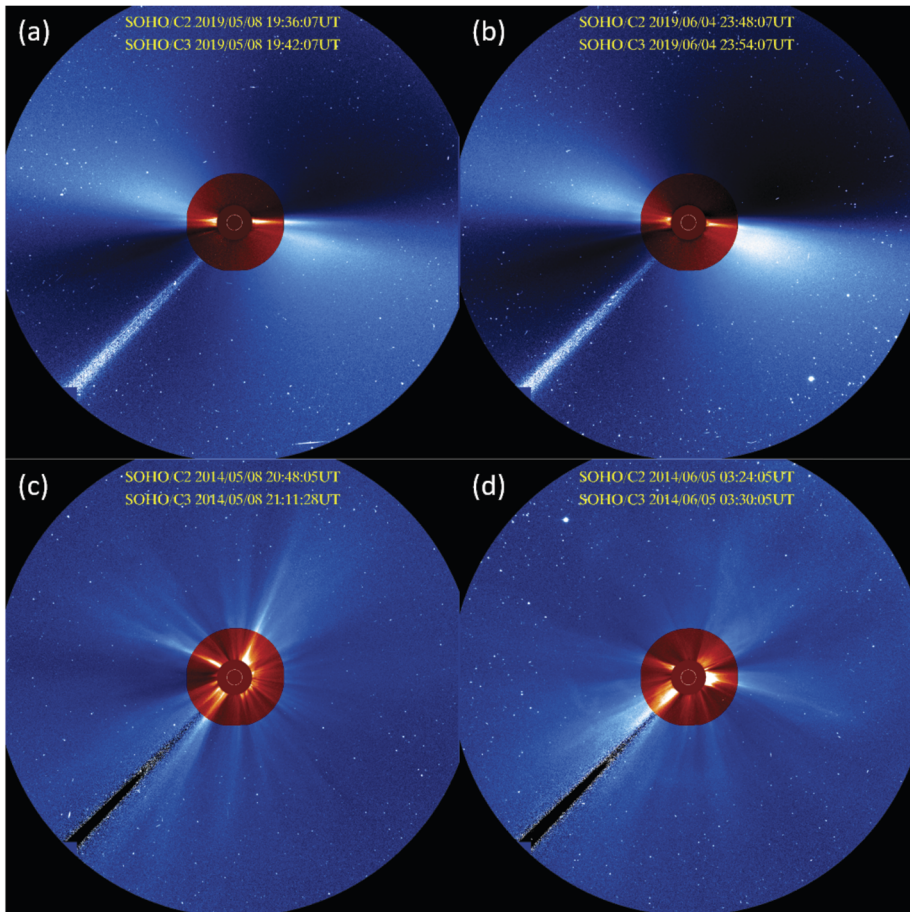
Figure 1 White-light images of the solar corona from the Large-angle Spectroscopic Coronagraph (LASCO) instrument on board the SOHO spacecraft. Panels **a** and **b** show images 27 days apart close to solar minimum, while panels **c** and **d** show images 27 days apart close to solar maximum.

27 days after panel a. These images were taken in mid-2019, close to solar minimum. The streamers, associated with the slow solar wind, are confined to the equatorial regions in both cases and there does not appear to be substantial evolution between the two time periods. Panels c and d show the same for 2014, close to solar maximum. Streamers are present at all latitudes in both images, but the locations and widths have changed substantially over the 27-day period.

The rate of change of solar-wind structure is also important for a second aspect of space-weather forecasting. Assimilation of in situ observations into solar-wind models (Lang et al., 2017; Lang and Owens, 2019) has been shown to provide a significant improvement to forecast accuracy (Lang et al., 2021). Remote-sensing observations, such as interplanetary scintillation (Jackson et al., 2015) and, in principle, information from white-light heliospheric imager observations (Barnard et al., 2019, 2020) can also be used. This data assimilation (DA) process requires an estimate of the observation uncertainty. A small part of this uncer-

tainty is the measurement error, but more significant is the representivity error. This quantifies how well the observations match up with the properties represented by the model.

For in situ observations, any latitudinal offset, $\Delta\theta$, between the point of observation and the latitude being forecast will introduce a spatial observational error (Owens et al., 2020). There is also a temporal aspect to the observation error, best understood through an example. A spacecraft at the L5 Lagrange point, approximately 60° behind Earth in its orbit, would observe the solar-wind conditions expected to arrive at Earth in approximately 5 days time (Simunac et al., 2009; Thomas et al., 2018), assuming no time evolution of the coronal solar-wind sources and hence 1-AU structure (this also ignores the $\Delta\theta$ effect due to the inclination of the ecliptic plane to the solar equator, Owens et al., 2019). Both the near-Earth and the L5 observations contain useful information about the solar-wind structure and hence assimilating these data should (and, in general, does) improve forecasting (Lang et al., 2021). Let us suppose that we want to forecast near-Earth solar-wind conditions three days ahead. Earth's Carrington longitude in three days time will be the same as that observed at L5 two days previously, and as that last observed at Earth $27.27 + 3 = 30.27$ days previously. Intuitively, we expect that the newer observation will be of greater value to the DA than the older observation. Hence, a naive approach would be to only use the most recent observation. More desirable would be to use both observations, but to quantitatively weight the observations by their relative merit. At present, however, these weightings are unknown. In particular, it is not clear whether newer observations should be more valued at solar minimum than at maximum, when the corona and hence solar-wind structure is known to be more dynamic. Studies of observation impact within DA can shed light on which observations influence the quality of the forecast (Fowler and van Leeuwen, 2013; Langland and Baker, 2004). However, these efforts in their infancy for solar-wind DA.

This study aims to quantify the rate of change in solar-wind structure at 1 AU using two key parameters: the solar-wind speed, V, and the radial magnetic-field component, B_R. These two parameters are chosen as they characterise the ambient solar wind well, representing both the plasma flow and the large-scale heliospheric magnetic-field structure. They are also the parameters that are passed from coronal to heliospheric models and the most critical parameters for solar-wind DA. Section 2 uses in situ solar-wind observations, while Section 3 uses magnetogram-constrained coronal and heliospheric simulations. As properties at 1 AU are directly (though not linearly) related to properties at the top of the corona, the results for 1-AU conditions are expected to be representative of the coronal variation (and vice versa). Analysis is performed at 1 AU for two reasons. First, there is a long record of in situ observations at this location, which enables a 'sanity check' on the results obtained from simulations. Secondly, for DA purposes, we require the variability to be quantified at the observation distance of 1 AU.

2. In Situ Spacecraft Observations

Multi-spacecraft observations provide a means of assessing the time evolution of the solar-wind structure. Of particular value are pairs of observations at the same solar latitudes and radial distances, but separated in longitude by an angle $\Delta\phi$. In this case, due to solar rotation, the spacecraft will observe the same Carrington longitude at a time difference given by $\Delta\phi / \Omega$, where Ω is the angular rotation speed of the Sun. Any difference between the solar-wind properties observed at the two spacecraft then equates solely to the time evolution of the solar-wind structure at the observation distance, r. For long time scales (i.e. 1 hour and above, as considered in this study), this is primarily the result of changes in the solar-wind
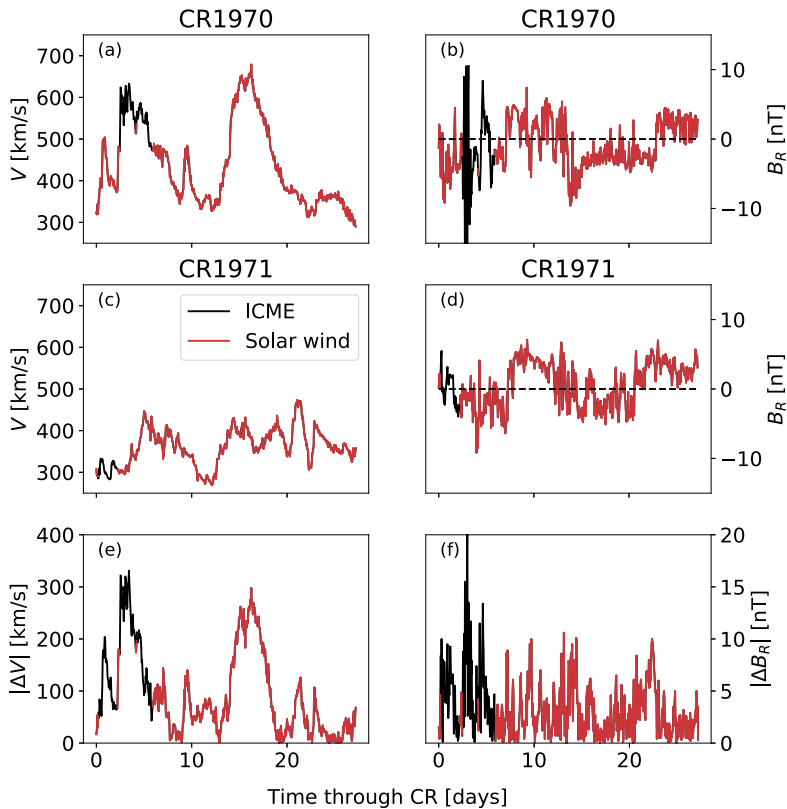
Figure 2 Near-Earth solar-wind observations as a function of time through Carrington rotations 1970 (panels **a** and **b**) and 1971 (panels **c** and **d**). This period spans from 23 November 2000 to 17 January 2001. Solar-wind speed, V (**a** and **c**) and radial magnetic field, B_R (**b** and **d**) are shown, with times identified as ICMEs in black. Panels **e** and **f** show the absolute difference between the two Carrington rotations, $|\Delta V|$ and $|\Delta B_R|$, respectively.

sources. Deterministic in-transit effects, such as large-scale stream interactions, will produce the same conditions at r for the same solar-wind source structure. It is only stochastic in-transit processes between the corona and spacecraft, such as turbulence (Bruno and Carbone, 2005), that can produce different conditions at r for the same solar-wind sources, but these differences are likely to be at smaller temporal/spatial scales than considered here.

The STEREO (Solar Terrestrial Relations Observatory) mission, launched in 2007 (Kaiser, 2005), consists of two spacecraft in Earth-like orbits about the Sun. They separated ahead and behind the Earth in its orbit by 22° per year. Thus, the STEREO spacecraft, in conjunction with near-Earth spacecraft, provide a close approximation to the 'ideal' dataset described above. However, due to orbits being in the ecliptic plane (which is inclined to the solar equator by an angle of 7.25°, resulting in differences in solar latitude between spacecraft) and the longitudinal separation of the spacecraft progressing in step with the solar cycle, it is difficult to isolate the effects of time evolution, latitudinal differences and the solar cycle from this dataset (Turner et al., 2021).

Instead, we here use only the OMNI dataset of near-Earth solar-wind observations (King and Papitashvili, 2005). Earth encounters the same Carrington longitude every 27.27 days.

This is the basis for so-called 'recurrence' (or '27-day persistence') forecasts of the solar wind (e.g. Bartels, 1934; Owens et al., 2013). Between such consecutive observations, Earth also moves in solar latitude by an angle $\Delta\theta$. Thus, a difference in solar-wind properties could be the result of time evolution and/or spatial structure in latitude. Over 27.27 days, Earth has $\Delta\theta \leq 3.5°$, thus we expect the $\Delta\theta$ effect on the observed solar-wind properties to be relatively small (Owens et al., 2019; Laker et al., 2021; Turner et al., 2021).

Figure 2 shows an example of the evolution of near-Earth solar-wind structure over consecutive Carrington rotation (CR) numbers 1970 and 1971. This interval spans 23 November 2000 to 17 January 2001 and thus is close to solar maximum. The data are plotted as time through the CR, allowing the same Carrington longitudes to be directly compared. The radial magnetic field, B_R, shows a somewhat similar four-sector structure in both CRs. Heliospheric current sheet (HCS) crossings, seen as persistent changes in B_R polarity, occur around days 1, 7, 12 and $20-22$ through the CR. Looking at the magnitude of the difference in B_R between the two CRs, $|\Delta B_R|$, the largest sustained values are around the times of these HCS crossings, suggesting some evolution of the large-scale heliospheric magnetic-field structure. The exception to this is the period of large $|\Delta B_R|$ around days 0 to 6. These periods have been independently identified as ICMEs (Richardson and Cane (2010); see also https://izw1.caltech.edu/ACE/ASC/DATA/level3/icmetable2.htm). Such transient disturbances are not expected to repeat in successive Carrington rotations.

For the solar-wind speed, V, the difference between the two CRs is more marked. Slow solar-wind is present around the four HCS crossings in both CRs, but the two fast streams in CR 1970 are absent in CR 1971. The first fast stream in CR 1970, arriving around day 3, is likely to have been the result of an ICME and thus would not be expected to repeat in CR 1971. The second fast stream arriving on day 13, however, appears to be a change in the ambient solar-wind speed structure. Thus, even when removing ICMEs from the comparison, there is a large $|\Delta V|$ period around days 13 to 19.

Computing the average values across this particular Carrington rotation gives $<|\Delta V|>_{CR}=$ 95.4 km s^{-1}, reducing to 78.8 km s^{-1} when ICMEs are removed (i.e. removing the whole interval between the ICME first disturbance time and the ICME trailing-edge time listed in the Richardson and Cane, 2010 online catalogue), and $<|\Delta B_R|>_{CR}=$ 3.23 nT, reducing to 2.78 nT when ICMEs are removed.

Figure 3 shows the same analysis applied to the OMNI dataset over the period 21 November 1994 to 18 June 2020, for which there is near-complete data coverage. For solar-cycle context, the monthly sunspot number (SSN) is shown. We also construct a solar-activity index (SAI), aimed at characterising the progression of the solar cycle independent of the variation in sunspot-cycle amplitude:

$$\text{SAI}(t) = \frac{SSN_{13}(t)}{\max\left[SSN_{13}(t - 5.5 \text{ yr} : t + 5.5 \text{ yr})\right]}, \tag{1}$$

where $SSN_{13}(t)$ is the 13-month smoothed sunspot number centred on time t. It is computed as a rolling average at monthly intervals. This is normalised by the maximum SSN_{13} value in an 11-year window centred on t. Thus, by construction, SAI has a minimum value of 0 and reaches a maximum value of 1 in every solar cycle. Note that the 11-year window means that SAI can only currently be computed up to 2016. In order to extend the sequence, we assume that the sunspot number in the first half of Solar Cycle (SC) 25 will not exceed the maximum value of SC24. Given we are only concerned with SAI being above/below 0.5 to define high/low activity, and SAI has already dropped below 0.5 in late 2016, this assumption is highly unlikely to affect the results shown here.
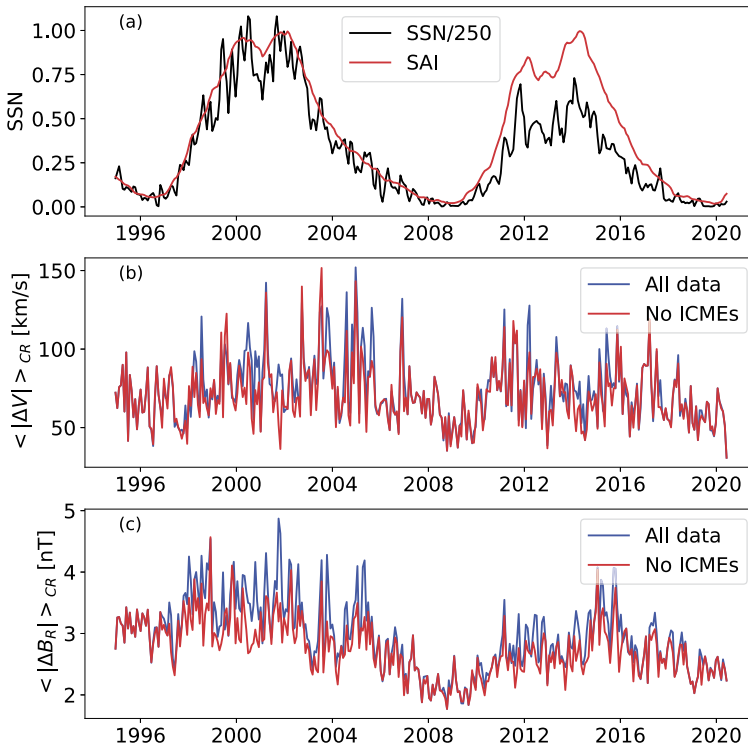
Figure 3 Time series of solar-wind properties over the period 1995–2020 using the OMNI dataset. (**a**) Monthly sunspot number (black), scaled by a factor 1/250 for plotting purposes. Also shown in red is the solar activity index (SAI) produced by scaling the 13-month smoothed sunspot number to the maximum value in an 11-year window. (**b**) $< |\Delta V| >_{CR}$, the average change in solar-wind speed over a Carrington rotation. (**c**) $< |\Delta B_R| >_{CR}$, the average change in radial magnetic field over a Carrington rotation. Blue lines show all data, red lines show values with ICMEs removed.

Using the OMNI dataset, the average change in solar-wind speed over a Carrington rotation, $< |\Delta V| >_{CR}$, varies from around 30 km s^{-1} to 150 km s^{-1} (see also Table 1). Whilst there is a great deal of scatter, there does appear to be a weak solar-cycle variation, quantified further below. Removing ICMEs from the data generally reduces $< |\Delta V| >_{CR}$, as expected. ICME removal produces a greater reduction in $< |\Delta V| >_{CR}$ at times of high solar activity than low, as there are simply more ICMEs at that time (Richardson and Cane, 2010). Thus, the effect of removing ICMEs is to reduce the overall solar-cycle variation (see also Kohutova et al., 2016).

For the radial magnetic field, $< |\Delta B_R| >_{CR}$ varies between approximately 2 and 5 nT. There is a more obvious solar-cycle trend. Also, note that $< |\Delta B_R| >_{CR}$ is generally lower in SC24 than during the larger-amplitude SC23. Again, the effect of removing ICMEs is to reduce $< |\Delta B_R| >_{CR}$ preferentially at solar maximum and hence reduce the overall solar-cycle trend.

Table 2 summarises the linear correlation coefficient (r_L) and the Spearman rank-ordered correlation coefficient (r_S) with both SSN and SAI. Using a Fisher r-to-z transformation (Press et al., 1989) with N = 342, all reported correlations are found to be significant (strictly speaking, the probability is below 1% that the reported correlation is consistent with zero for the given sample size).

Table 1 Mean values of $< |\Delta V| >_{CR}$ and $< |\Delta B_R| >_{CR}$ for both OMNI data and HelioMAS (Riley et al., 2012). Uncertainty ranges are one standard error on the mean.

	OMNI data 1995 – 2020		HelioMAS 1975 – 2020	
	All data	No ICMEs	Global	Ecliptic
$< |\Delta V| >$ km s^{-1} (all)	73.7 +/− 1.1	70.2 +/− 1.0	57.8 +/− 1.5	79.2 +/− 1.2
$< |\Delta V| >$ km s^{-1} (SAI <= 0.5)	71.5 +/− 1.8	68.5 +/− 1.5	38.4 +/− 1.1	82.0 +/− 1.6
$< |\Delta V| >$ km s^{-1} (SAI > 0.5)	79.7 +/− 1.7	74.2 +/− 1.8	91.8 +/− 2.0	74.3 +/− 1.6
$< |\Delta B_R| >$ nT (all)	2.94 +/− 0.02	2.75 +/− 0.02	0.47 +/− 0.01	0.96 +/− 0.01
$< |\Delta B_R| >$ nT (SAI <= 0.5)	2.81 +/− 0.05	2.69 +/− 0.04	0.33 +/− 0.01	0.84 +/− 0.02
$< |\Delta B_R| >$ nT (SAI >0.5)	3.22 +/− 0.05	2.91 +/− 0.04	0.70 +/− 0.01	1.16 +/− 0.02

Table 2 Correlation coefficients of $< |\Delta V| >_{CR}$ and $< |\Delta B_R| >_{CR}$ with SSN and SAI. Linear correlation coefficients (r_L) are shown with Spearman rank-ordered correlation coefficient (r_S) in parentheses.

	r_L (r_S)	SSN	SAI
OMNI observations	$< |\Delta V| >_{CR}$ (All data)	0.37 (0.45)	0.28 (0.34)
	$< |\Delta V| >_{CR}$ (no ICMEs)	0.25 (0.30)	0.17 (0.19)
	$< |\Delta B_R| >_{CR}$ (All data)	0.60 (0.63)	0.46 (0.49)
	$< |\Delta B_R| >_{CR}$ (no ICMEs)	0.47 (0.50)	0.33 (0.35)
HelioMAS simulations	$< |\Delta V| >_{CR}$ (Global)	0.67 (0.69)	0.74 (0.74)
	$< |\Delta V| >_{CR}$ (Ecliptic)	−0.16 (−0.14)	−0.22 (−0.20)
	$< |\Delta B_R| >_{CR}$ (Global)	0.83 (0.85)	0.80 (0.82)
	$< |\Delta B_R| >_{CR}$ (Ecliptic)	0.58 (0.66)	0.44 (0.49)

Figure 4 summarises the distributions of $< |\Delta V| >_{CR}$ and $< |\Delta B_R| >_{CR}$ for different divisions of the data. Box and whisker plots are used, where the white line shows the median, the coloured area spans with interquartile range (IQR) and the thin line spans the maximum to minimum values excluding outliers (i.e. 1.5 IQR above and below the third and first quartiles, respectively). The notch about the median shows the 95% confidence interval on the median.

A number of features are worth noting. First, $< |\Delta B_R| >_{CR}$ exhibits a stronger correlation with both measures of the solar cycle than $< |\Delta V| >_{CR}$. Secondly, the correlation of both $< |\Delta B_R| >_{CR}$ and $< |\Delta V| >_{CR}$ with SSN is stronger than the equivalent with SAI. From this we infer that the amplitude – as well as phase – of the solar cycle affects the observed rate of change of the solar-wind structure.

Taking SAI $= 0.5$ as the threshold between low and high solar activity, both $< |\Delta V| >_{CR}$ and $< |\Delta B_R| >_{CR}$ show significantly higher values during high SAI. However, the magnitude of this solar-cycle variation is small (of the order of 10%); see also Table 1.

For both $< |\Delta V| >_{CR}$ and $< |\Delta B_R| >_{CR}$, removing ICMEs further reduces the magnitude of the observed relation between solar-wind
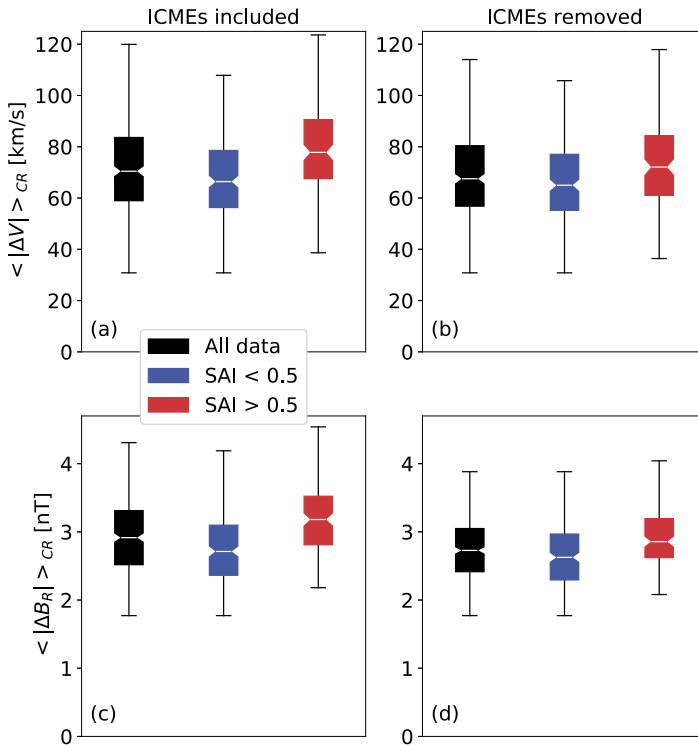
Figure 4 Box and whisker plots summarising the distributions of $< |\Delta V| >_{CR}$ (panels **a** and **b**) and $< |\Delta B_R| >_{CR}$ (**c** and **d**) obtained from consecutive 27-day intervals of OMNI observations. The white line shows the median, the coloured area spans with interquartile range (IQR), and the thin line spans the maximum to minimum values excluding outliers (i.e. 1.5 IQR above and below the third and first quartiles, respectively). The notch about the median shows the 95% confidence interval on the median. The left-hand panels (**a** and **c**) show all OMNI data for the period 21 November 1994 to 18 June 2020, the right-hand panels (**b** and **d**) show the same period with ICMEs removed. Black, blue, and red show all, low, and high solar-activity levels, respectively.

variability and solar cycle is the result of increased occurrence of transient ICMEs at solar maximum. Whilst the differences between high and low activity remain statistically significant, for the ICME-removed series, $< |\Delta V| >_{CR}$ and $< |\Delta B_R| >_{CR}$ increase by only 8% between low and high solar activity.

Using the OMNI dataset we cannot completely remove the effect of latitudinal offset, $\Delta\theta$ (see also Turner et al., 2021) or transients resulting from either unidentified ICMEs and/or turbulent and mesoscale structures (Viall, DeForest, and Kepko, 2021; Verscharen, Klein, and Maruca, 2019). Thus, it is useful to also examine simulation results that attempt to capture only the ambient solar wind. This also allows a more global picture of changing solar-wind structure.

3. Solar-Wind Simulations

Global coronal models, constrained by the photospheric magnetic observations, are typically used to approximate the steady-state corona. These coronal solutions can then be
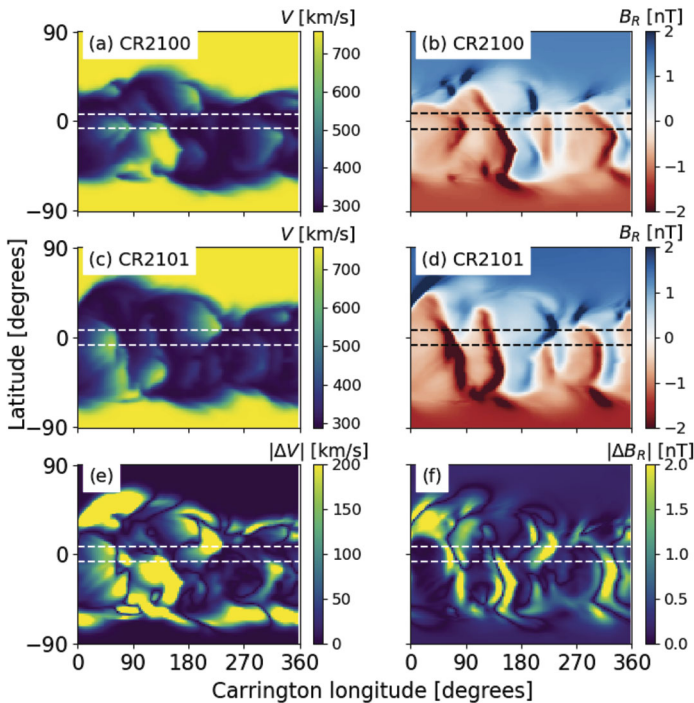
Figure 5 Latitude–longitude maps at a constant radius of 1 AU for heliospheric MHD solutions constrained by HMI magnetograms. Carrington rotations 2100 (panels **a** and **b**) and 2101 (panels **b** and **c**) are shown. Solar-wind speed, V, is shown in the left column, with radial magnetic field, B_R, on the right. The absolute difference between the two CRs is shown in panels **e** and **f**. Dashed horizontal lines span a latitude of $+/- 7.25°$ about the solar equator.

used to drive heliospheric models out to Earth orbit. Potential-field source surface (PFSS) models are intrinsically steady state (Altschuler and Newkirk, 1969; Schatten, Wilcox, and Ness, 1969), whereas models solving the time-dependent MHD equations are relaxed until a steady-state equilibrium is achieved. Indeed, triggering a CME-like eruption is often achieved by ad hoc modifications of the boundary conditions in order to energise the system (e.g. Torok et al., 2018).

This section uses archived output from the combined Magnetohydrodynamics Algorithm outside a Sphere (MAS: Linker et al., 1999) coronal and HelioMAS (Riley et al., 2012) solar-wind MHD models, using a range of photospheric observatories. All data used are available from https://www.predsci.com/mhdweb/home.php.

Example solutions at 1 AU for CRs 2100 and 2101 using magnetograms from the Helioseismic and Magnetic Imager (HMI: Scherrer et al., 2012) are shown in Figure 5. This period spans from 9 August 2010 to 3 October 2010 and thus is close to solar-minimum conditions. Both the V and B_R structures for the two CRs show a reasonable agreement at the global scale. In both CRs, fast wind is confined to the polar regions, with a broad band of slow wind spanning the equator, but slightly skewed towards the southern hemisphere. The HCS, seen as the white line separating opposite B_R polarities, shows two large excursions into the southern hemisphere around Carrington longitudes of 180° and 330° in both CRs.

Taking the difference between consecutive steady-state coronal solutions has previously been used as a method to identify regions of coronal evolution (Luhmann et al., 1998, 1999).
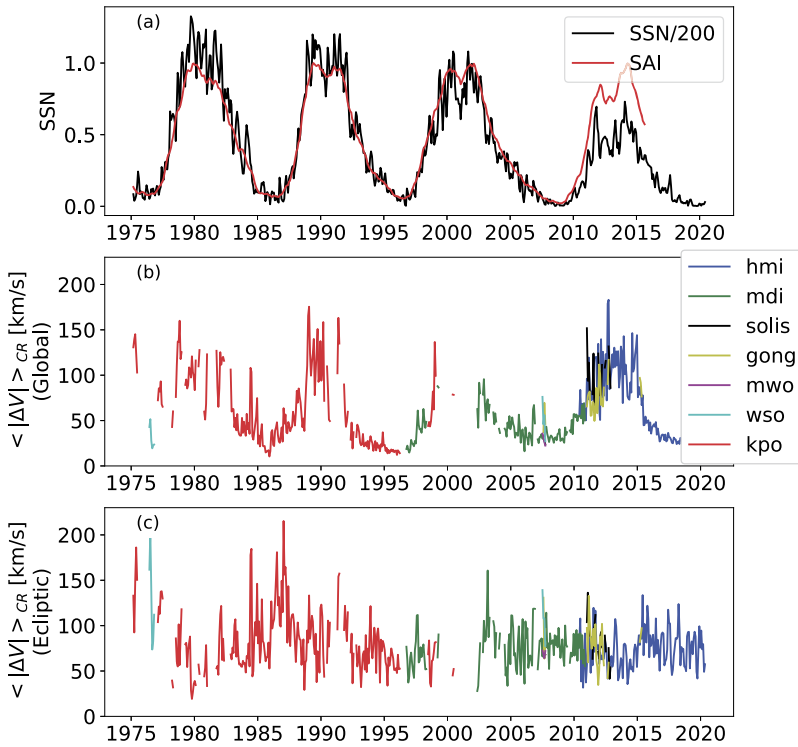
Figure 6 Time series of $< |\Delta V| >_{CR}$ from consecutive CRs obtained from HelioMAS MHD simulations at 1 AU. (**a**) Scaled monthly sunspot number and the solar-activity index, shown for solar-cycle context. (**b**) $< |\Delta V| >_{CR}$ averaged over all latitudes. The colour coding for different observatories is given in the legend. See https://www.predsci.com/mhdweb/home.php for more details. (**c**) $< |\Delta V| >_{CR}$ averaged over the $+/- 7.25°$ about the solar equator.

This evolution has been associated with CMEs, suggesting coronal eruptions may be a way in which the corona transitions between quasi-steady-state conditions (see also Low, 2001; Owens and Crooker, 2006; Owens et al., 2007). Here, we look at the change in the steady-state 1-AU solar-wind properties. Despite the global-scale agreement between CRs 2100 and 2101, Figures 5e and f show that there are nevertheless regions of large difference, in both V and B_R. These are most pronounced in the mid-latitudes. Around the ecliptic-plane latitudes – the band between -7.25 and $7.25°$ from the equator – $|\Delta V|$ is relatively suppressed, as both CRs largely show fairly uniform slow wind at those latitudes. $|\Delta B_R|$, on the other hand, shows similar values at mid-latitudes and the ecliptic.

Averaging over all latitudes and longitudes for this Carrington rotation, we find $< |\Delta V| >_{CR}= 73.0$ km s^{-1} and $< |\Delta B_R| >_{CR}= 0.509$ nT. When restricted to ecliptic longitudes, $< |\Delta V| >_{CR}$ drops by around a quarter to 58.2 km s^{-1}, whereas $< |\Delta B_R| >_{CR}$ increases to 0.888 nT.

Figures 6 and 7 show the same analysis applied to all available HelioMAS solutions, spanning the years 1974 to 2020. Magnetograms from a range of observatories are used, but $< |\Delta V| >_{CR}$ and $< |\Delta B_R| >_{CR}$ are only computed when HelioMAS solutions are available that are based on magnetograms from the same observatory for two consecutive CRs. For the purpose of computing average values over the whole time period, a composite series is
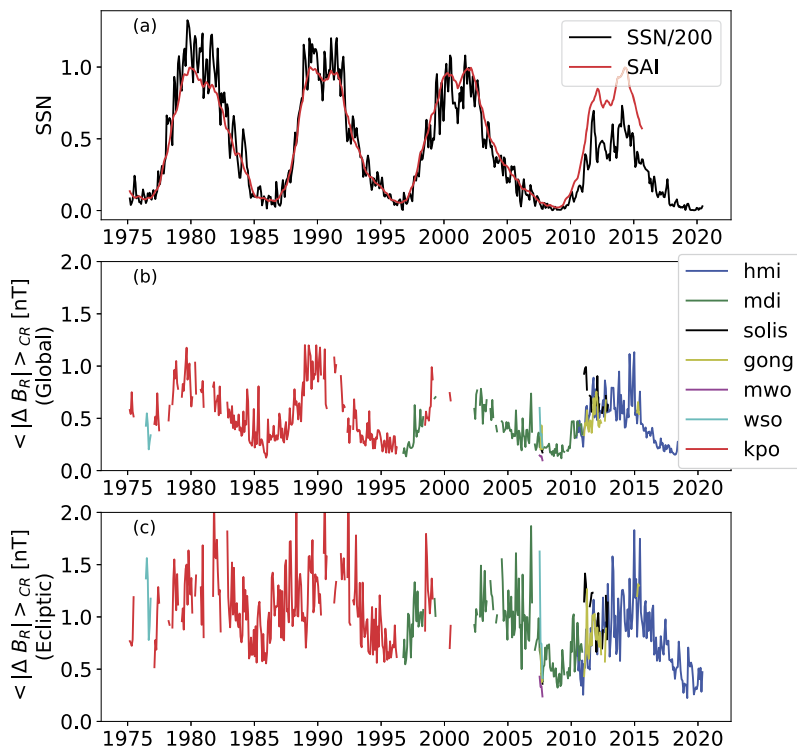
Figure 7   Same as Figure 6, but for $< |\Delta B_R| >_{CR}$, i.e. time series of $< |\Delta B_R| >_{CR}$ from consecutive CRs obtained from HelioMAS MHD simulations at 1 AU. (**a**) Scaled monthly sunspot number and the solar-activity index, for solar-cycle context. (**b**) $< |\Delta B_R| >_{CR}$ averaged over all latitudes. The colour coding for different observatories is given in the legend. See https://www.predsci.com/mhdweb/home.php for more detail. (**c**) $< |\Delta B_R| >_{CR}$ averaged over the $+/- 7.25°$ about the solar equator.

also produced. This uses all observatories, and when multiple observatories are available for the same interval, an average value of $< |\Delta V| >_{CR}$ and $< |\Delta B_R| >_{CR}$ is computed. These numbers are reported in Tables 1 and 2 and shown in Figure 8.

For solar-wind speed, the global (i.e. over all latitudes) average $< |\Delta V| >_{CR}$ ranges from approximately 20 to 150 km s^{-1}. There is a clear solar-cycle variation. Although there is a large data gap during SC23, there is not an obvious cycle-to-cycle variation in the peak values of global $< |\Delta V| >_{CR}$. For example, the low-amplitude SC24 shows similar $< |\Delta V| >_{CR}$ values to the large-amplitude SC19 (around 1980). This is supported by the correlation coefficients summarised in Table 2: the correlation of global $< |\Delta V| >_{CR}$ is stronger with SAI – which removes the effect of changing solar-cycle amplitude – than it is with SSN. This trend is opposite to that observed with the OMNI dataset, which suggests there may be an increased occurrence of unidentified transients in the OMNI dataset during strong solar cycles.

Limiting analysis to ecliptic latitudes, $+/- 7.25°$ about the solar equator, gives a different picture; there is little solar-cycle variation in $< |\Delta V| >_{CR}$. The average value of $< |\Delta V| >_{CR}$ at ecliptic latitudes is in approximate agreement with that obtained from the OMNI dataset.

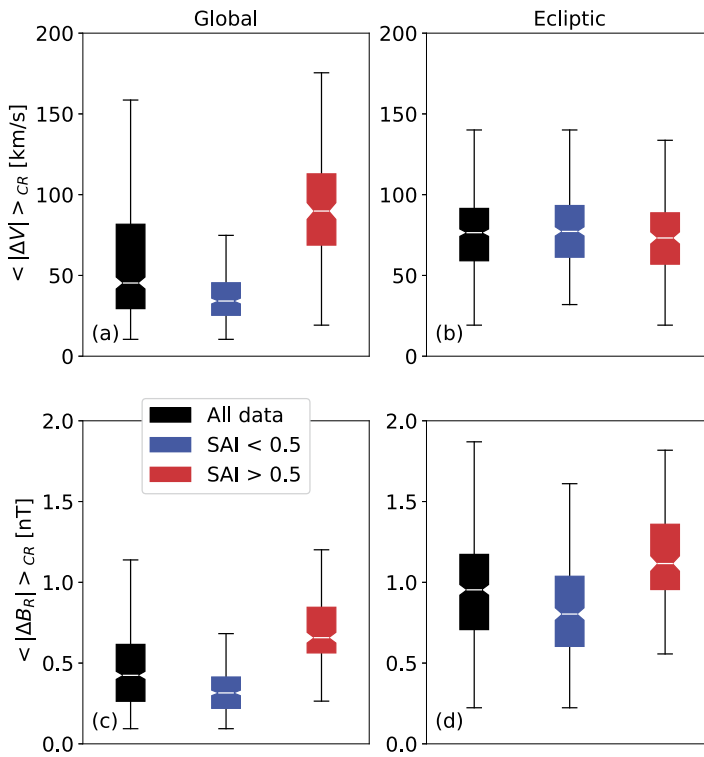**Figure 8** Box and whisker plots summarising the distributions of $< |\Delta V| >_{CR}$ (panels **a** and **b**) and $< |\Delta B_R| >_{CR}$ (**c** and **d**) obtained from consecutive solutions of HelioMAS at 1 AU. The white line shows the median, the coloured area spans with interquartile range (IQR), and the thin line spans the maximum to minimum values excluding outliers (i.e. 1.5 IQR above and below the third and first quartiles, respectively). The left-hand panels (**a** and **c**) show values averaged over all latitudes, the right-hand panels (**b** and **d**) show values at ecliptic latitudes (i.e. $+/-7.25°$ about the solar equator). Black, blue, and red show all, low, and high solar-activity levels, respectively.)

Global $< |\Delta B_R| >_{CR}$ shows a strong correlation with the solar cycle. As 1-AU $|B_R|$ is expected to be higher in higher-amplitude solar cycles (Lockwood, Stamper, and Wild, 1999; Solanki, Schüssler, and Fligge, 2000; Owens and Lockwood, 2012), it is perhaps unsurprising that the correlation of $< |\Delta B_R| >_{CR}$ is slightly higher with SSN than SAI. Confining this analysis to ecliptic latitudes, the correlation of $< |\Delta B_R| >_{CR}$ with both SSN and SAI is reduced, but still significant and of large amplitude. Note that the magnitude of $< |\Delta B_R| >_{CR}$ is lower than that obtained from the OMNI dataset, as magnetogram-based estimates of the heliospheric magnetic field are known to underestimate $|B_R|$ by around a factor two (Wallace et al., 2019; Linker et al., 2017, 2021)

Taking a threshold of SAI $= 0.5$, global $< |\Delta V| >_{CR}$ varies by a factor 2.39 between periods of low and high solar activity (i.e. a 139% increase during high activity). For $< |\Delta B_R| >_{CR}$, we find a factor 2.12 (i.e. a 112% increase during high activity). Restricting to ecliptic latitudes reduces these solar-cycle variations to 10% for $< |\Delta V| >_{CR}$ and 38% for $< |\Delta B_R| >_{CR}$. While still larger than the values found by analysis of the OMNI data, particularly for $< |\Delta B_R| >_{CR}$, these values are in closer agreement with the weak solar-cycle trends in in situ observations.
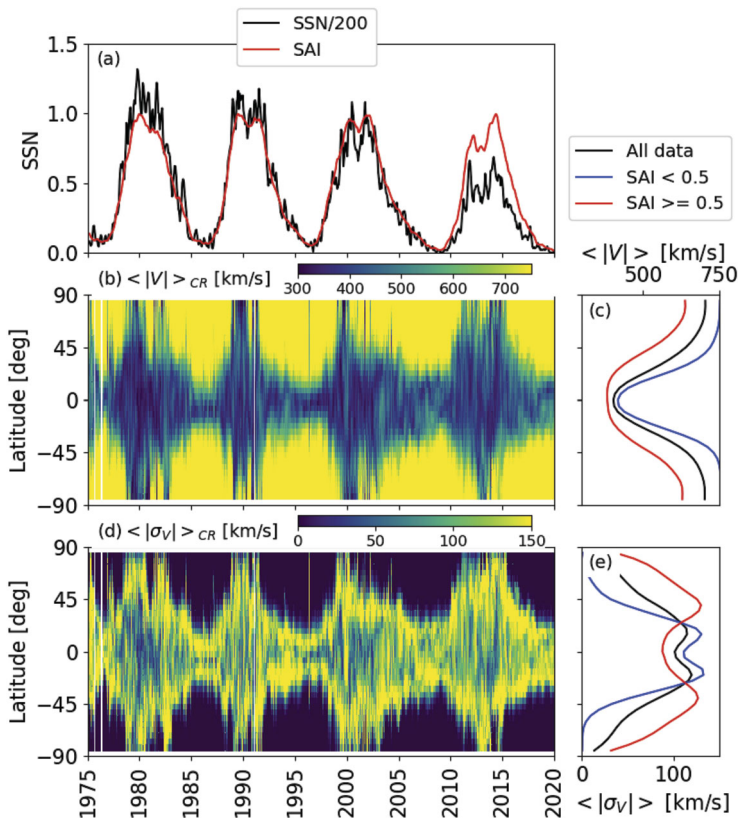
Figure 9 The latitudinal structure of the 1-AU solar-wind speed, V, from HelioMAS as a function of time. (**a**) Sunspot number and solar-activity index, for solar-cycle context. (**b**) The longitudinally averaged $|V|$ for each CR, $< |V| >_{CR}$, as a function of latitude and time. Panels **d** and **e** show the standard deviation of V within a CR, σ_V, as a function of latitude and time. This is a measure of the longitudinal structure in V for a given CR. Panels **c** and **e** show $< |V| >_{CR}$ and σ_V as a function of latitude and averaged over all times (black), low solar activity (blue), and high solar activity (red).

4. The Role of Latitude

In order to better understand the difference between global and ecliptic estimates of $< |\Delta V| >_{CR}$ and $< |\Delta B_R| >_{CR}$, it is useful to further investigate the latitudinal structure of both the solar-wind properties and their rate of change.

Figure 9 shows how V varies with latitude and time. Panel b shows longitudinal averages of V over a CR (see also Figure 4a of Owens, Lockwood, and Riley, 2017). This is in close agreement with the structure observed both in situ (McComas et al., 2003) and via radio scintillation (Manoharan, 2012). At solar minimum, there is slow wind around the solar equator and uniform fast wind at the mid- and high latitudes. At solar maximum, slow wind extends to all latitudes.

Figure 9e shows σ_V, the standard deviation in V over a Carrington rotation. This is a measure of the degree of longitudinal structure in V. At times and latitudes with uniform fast wind, $\sigma_V = 0$. However, σ_V is also relatively low at latitudes and times where slow wind completely dominates, such as near the equator during solar maximum. The highest values
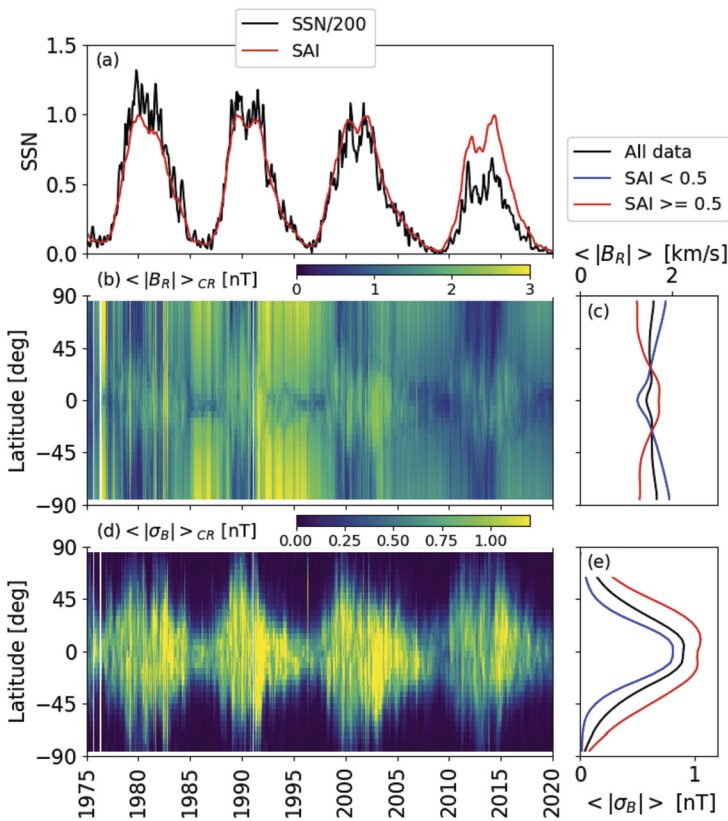
Figure 10 The latitudinal structure of the 1-AU radial magnetic field, B_R, from HelioMAS as a function of time. (**a**) Sunspot number and solar-activity index, for solar-cycle context. (**b**) The longitudinally averaged $|B_R|$ for each CR, $<|B_R|>_{CR}$, as a function of latitude and time. Panels **d** and **e** show the standard deviation of B_R within a CR, σ_B, as a function of latitude and time. This is a measure of the longitudinal structure in B_R for a given CR. Panels c and e show $<|B_R|>_{CR}$ and σ_B as a function of latitude and averaged over all times (black), low solar activity (blue), and high solar activity (red).

of σ_V are produced at latitudes that contain both fast and slow wind, right at the transition between the two solar-wind regimes.

Figure 10 shows the same analysis for B_R. Panels b and c show that $<|B_R|>_{CR}$ does not show a large variation in either latitude or time. Conversely, σ_B, shown in panels d and e, shows a somewhat similar variation to σ_V; it is effectively zero at high latitudes during low solar activity, with large values extending to higher latitudes at high solar activity. The main difference from σ_V, however, is that σ_B remains high at the equator throughout the solar cycle. This is because large σ_B is effectively a marker for latitudes and times where B_R changes polarity. It will thus be maximised at the equator as the HCS is, on average, centred at the equator (see, however, Mursula and Hiltula, 2003), with high-latitude excursions becoming more common at solar maximum (e.g. Smith, 1990). Thus, mixed magnetic polarities (and high σ_B) are always present at the equator (see also Figure 13 of Owens and Forsyth, 2013).

With this global context in mind, we now consider how the rate of change of the solar wind varies as a function of latitude. Figure 11 shows $<|\Delta V|>_{CR}$ and $<|\Delta B_R|>_{CR}$
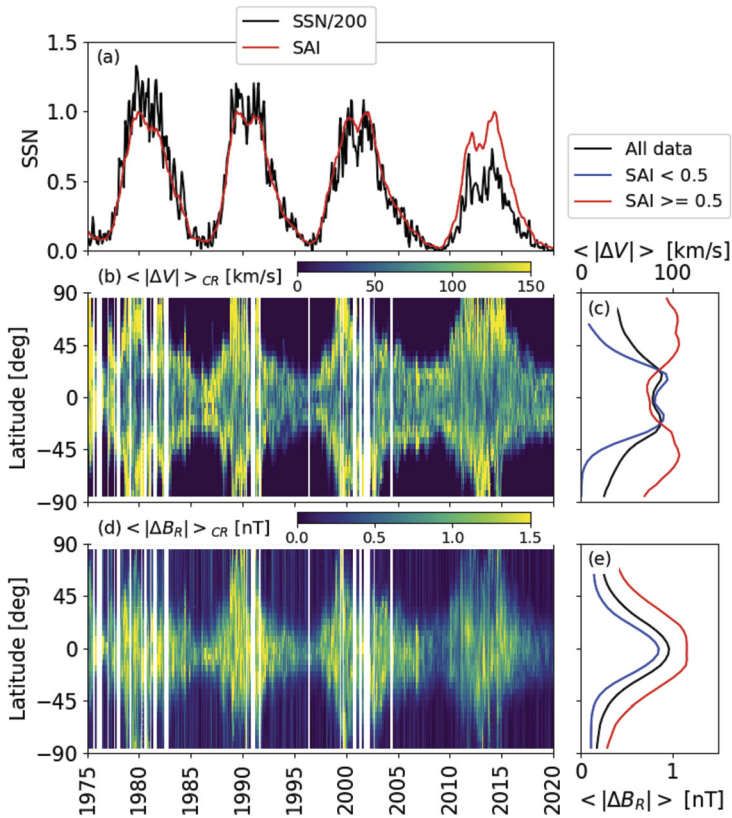
Figure 11 The effect of latitude on $<|\Delta V|>_{CR}$ (**b** and **c**) and $<|\Delta B_R|>_{CR}$ (**d** and **e**) from HelioMAS MHD simulations at 1 AU. (**a**) Time series of scaled SSN and SAI over the period 1975 to 2020. (**b**) $<|\Delta V|>_{CR}$ as a function of latitude and time. Panel **d** shows the same for $<|\Delta B_R|>_{CR}$. Panels **c** and **e** show $<|\Delta V|>_{CR}$ and $<|\Delta B_R|>_{CR}$, respectively, as a function of latitude and averaged over all times (black), low solar activity (blue), and high solar activity (red).

with latitude and time. Figure 11b shows that the overall envelope of (longitudinally averaged) $<|\Delta V|>_{CR}$ closely follows that of $<|V|>_{CR}$. High latitudes around solar minimum contain pure fast wind. As fast wind in HelioMAS simulations has uniform characteristics, $<|\Delta V|>_{CR}= 0$ km s^{-1} at these times and locations. With increasing solar activity, slow wind extends to higher latitudes. The variability of the slow wind means $<|\Delta V|>_{CR}> 0$ km s^{-1} at any latitude that contains some slow wind. The very highest values of $<|\Delta V|>_{CR}$ occur on the boundary of fast and slow winds, closely following σ_V. This is due to V at a given longitude changing between one regime and the other between consecutive CRs, and generating high $|\Delta V|$ as the precise location and timing of that transition evolves.

Splitting the data into high- and low-activity periods using a threshold of SAI $= 0.5$ shows this behaviour more clearly. In Figure 11c, $<|\Delta V|>_{CR}$ during high activity is approximately constant with latitude at around 100 km s^{-1}, with a slight decrease at the equator. This decrease is due to a near-complete absence of fast wind at these times/locations, reducing the possible variation (as seen by the decrease in V and σ_V at the equator during solar maximum). At low activity, however, a strong latitudinal variation in $<|\Delta V|>_{CR}$ is

present. $< |\Delta V| >_{CR}$ reaches around 100 km s^{-1} around the equator, similar to the high-activity value. Thus, the correlation of $< |\Delta V| >_{CR}$ with the solar cycle is low at the equator and high at the poles, as reported in Table 2.

$< |\Delta B_R| >_{CR}$ peaks at the equator throughout the solar cycle, but the maximum amplitude is higher at times of high solar activity than low. The amplitude variation is largely due to $< |B_R| >$ varying with solar activity. Thus, the correlation of $< |\Delta B_R| >_{CR}$ with SSN is high (> 0.4) at all latitudes.

5. Discussion

In this study we have quantified the rate of change of the ambient solar-wind structure over consecutive Carrington rotations (i.e. 27-day periods). This is important for both understanding the degree to which the steady-state approximation is valid, and is required in order to best exploit the available in situ solar-wind observations for data assimilation.

The first approach was to use solar-wind speed, V, and radial magnetic-field component, B_R, observed in near-Earth space using the OMNI dataset. By looking at the differences in consecutive Carrington rotations (CRs), we computed the changes in solar-wind properties at the same solar longitude, $|\Delta V|$ and $|\Delta B_R|$. A weak solar-cycle trend was found in the Carrington rotation averages of both these properties, $< |\Delta V| >_{CR}$ and $< |\Delta B_R| >_{CR}$. This could be partly attributed to the increased occurrence of interplanetary coronal mass ejections (ICMEs) at high solar activity. This is expected, as transient disturbances – by definition – do not repeat in each CR. After removing ICMEs there was only an 8% difference in high and low solar activity values of $< |\Delta V| >_{CR}$ and $< |\Delta B_R| >_{CR}$ for the ambient solar wind. This result appears to contradict the idea that coronal (and hence solar-wind) structure varies much more at solar maximum than minimum.

To obtain more of a global picture of solar-wind structure, the second half of the study used coronal and heliospheric MHD simulations constrained using the observed photospheric magnetic field. Such simulations are steady state and approximate the ambient solar-wind conditions only (CMEs are typically added as an additional, time-varying perturbation, e.g. Odstrcil, Riley, and Zhao, 2004). Globally, both $< |\Delta V| >_{CR}$ and $< |\Delta B_R| >_{CR}$ show a very strong correlation with solar activity, both in terms of the statistical significance of the relation and the magnitude of the effect (around a factor two). Restricting the analysis to ecliptic latitudes drastically reduces this trend, to 10% for $< |\Delta V| >_{CR}$ and to 38% for $< |\Delta B_R| >_{CR}$. Whilst these values are still higher than those obtained from the in situ observations, they are in much closer agreement.

Thus globally, the rate of change of solar-wind speed structure does correlate with the solar cycle, as expected. Specifically, $< |\Delta V| >_{CR}$ correlates more closely with the phase of the solar cycle than with sunspot number, which is determined by both phase and solar-cycle amplitude. Given solar-wind speed is partially ordered by the position of the heliospheric current sheet (HCS), this agrees with the findings that the average HCS position is a function of solar-cycle phase, but not solar-cycle amplitude (Alanko-Huotari et al., 2007; Owens and Lockwood, 2012). Note, however, that this relation may break down in very weak cycles (Owens, Lockwood, and Riley, 2017), possibly due to weakening of the photospheric magnetic field and the relation between coronal magnetic-field topology and solar-wind speed (Wang and Sheeley, 1990; Riley, Linker, and Arge, 2015).

Conversely, the global variability in the radial field is more closely correlated with the sunspot number than solar-cycle phase alone. This is likely the result of heliospheric radial magnetic-field strength varying closely with sunspot-cycle magnitude, as seen through solar

open solar flux reconstructions (Lockwood, Stamper, and Wild, 1999; Solanki, Schüssler, and Fligge, 2000; Krivova, Balmaceda, and Solanki, 2007; Owens and Lockwood, 2012).

$< |\Delta V| >_{CR}$ generally peaks at mid-latitudes, where slow and fast winds often coexist, giving the possibility of the largest $|\Delta V|$ values. At the equator, fast wind is more rarely present, reducing the possibility of large $|\Delta V|$. Conversely, $< |\Delta B_R| >_{CR}$ peaks at the equator, owing to the HCS – and hence mixed B_R polarity – being centred at the equator.

For the purposes of solar-wind data assimilation, it is necessary to relate the reliability of observations to their age. The results presented here suggest that, at least for in-ecliptic in situ observations, it is not necessary to assume that the rate at which observations become less reliable is a function of the solar cycle. Instead, we suggest simply using an 'age' uncertainty in solar-wind speed of around 70 km s^{-1} per CR (i.e. 3 km s^{-1} per day) since the observation was made, and 3 nT per CR (i.e. 0.1 nT per day) for the radial magnetic field. These would be added to other contributions to the representivity error. For observations from higher latitudes, such as from interplanetary scintillation or heliospheric imager observations, this age uncertainty is more strongly solar-cycle dependent.

Data Availability OMNI data are available from https://omniweb.gsfc81.nasa.gov/. The updated Cane and Richardson near-Earth CME list is available from http://www.srl.caltech.edu/ACE/ASC/DATA/level3/icmetable2.htm. Sunspot data are provided by the Royal Observatory of Belgium SILSO and available from www.sidc.be/silso/DATA/SN_m_tot_V2.0.csv. HelioMAS data is available from https://www.predsci.com/mhdweb/home.php.

All analysis and visualisation code is packaged with all required OMNI data here: www.github.com/University-of-Reading-Space-Science/SolarWindVariability. Routines are provided to automatically download and process the required HelioMAS data.

Declarations

Disclosure of Potential Conflicts of Interest We declare we have no conflicts of interest.

References

Alanko-Huotari, K., Usoskin, I.G., Mursula, K., Kovaltsov, G.A.: 2007, Cyclic variations of the heliospheric tilt angle and cosmic ray modulation. *Adv. Space Res.* **40**, 1064. DOI.

Altschuler, M.D., Newkirk, G.: 1969, Magnetic fields and the structure of the solar corona. *Solar Phys.* **9**, 131.

Antonucci, E., Harra, L., Susino, R., Telloni, D.: 2020, Observations of the solar corona from space. *Space Sci. Rev.* **216**, 117. DOI.

Arge, C.N., Odstrcil, D., Pizzo, V.J., Mayer, L.R.: 2003, Improved method for specifying solar wind speed near the Sun. *AIP Conf. Proc.* **679**, 190. DOI.

Barnard, L.A., Owens, M.J., Scott, C.J., Jones, S.R.: 2019, Extracting inner-heliosphere solar wind speed information from heliospheric imager observations. *Space Weather* **17**, 925. DOI.

Barnard, L., Owens, M.J., Scott, C.J., de Koning, C.A.: 2020, Ensemble CME modeling constrained by heliospheric imager observations. *AGU Adv.* **1**, e2020AV000214. DOI. eprint: https://onlinelibrary.wiley.com/doi/pdf/10.1029/2020AV000214.

Bartels, J.: 1934, Twenty-seven day recurrences in terrestrial-magnetic and solar activity, 1923–1933. *Terr. Magn. Atmos. Electr., J. Geophys. Res.* **39**, 201. DOI.

Breen, A.R., Moran, P.J., Varley, C.A., Wilkinson, W.P., Williams, P.J.S., Coles, W.A., Lecinski, A., Markkanen, J.: 1998, Interplanetary scintillation observations of interaction regions in the solar wind. *Ann. Geophys.* **16**, 1265. DOI. Publisher: Copernicus GmbH.

Brueckner, G.E., Howard, R.A., Koomen, M.J., Korendyke, C.M., Michels, D.J., Moses, J.D., Socker, D.G., Dere, K.P., Lamy, P.L., Llebaria, A., Bout, M.V., Schwenn, R., Simnett, G.M., Bedford, D.K., Eyles, C.J.: 1995, The Large Angle Spectroscopic Coronagraph (LASCO). *Solar Phys.* **162**, 357. DOI.

Bruno, R., Carbone, V.: 2005, The solar wind as a turbulence laboratory. *Living Rev. Solar Phys.* **2**, 4. DOI.

Cargill, P.J.: 2004, On the aerodynamic drag force acting on coronal mass ejections. *Solar Phys.* **221**, 135. DOI.

Case, a.W., Spence, H.E., Owens, M.J., Riley, P., Odstrcil, D.: 2008, Ambient solar wind's effect on ICME transit times. *Geophys. Res. Lett.* **35**, L15105. DOI.

Chollet, E.E., Giacalone, J.: 2011, Evidence of confinement of solar-energetic particles to interplanetary magnetic field lines. *Astrophys. J.* **728**, 64. DOI.

DeVore, C.R., Antiochos, S.K.: 2008, Homologous confined filament eruptions via magnetic breakout. *Astrophys. J.* **680**, 740. DOI.

Fowler, A., van Leeuwen, P.J.: 2013, Observation impact in data assimilation: the effect of non-Gaussian observation error. *Tellus, Ser. A Dyn. Meteorol. Oceanogr.* **65**, 20035. DOI.

Gosling, J.T.: 1993, The solar flare myth. *J. Geophys. Res.* **98**, 18937. DOI.

Hickmann, K.S., Godinez, H.C., Henney, C.J., Arge, C.N.: 2015, Data assimilation in the ADAPT photospheric flux transport model. *Solar Phys.* **290**, 1105. DOI.

Hoeksema, J.T., Scherrer, P.H.: 1986, Solar magnetic field, 1976 through 1985: an atlas of photospheric magnetic field observations and computed coronal magnetic fields from the John M. Wilcox Solar Observatory at Sanford, 1976–1985. NASA STI/Recon Technical Report N 86, 29760.

Jackson, B.V., Odstrcil, D., Yu, H., Hick, P.P., Buffington, A., Mejia-Ambriz, J.C., Kim, J., Hong, S., Kim, Y., Han, J.: 2015, The UCSD kinematic IPS solar wind boundary and its use in the ENLIL 3-D MHD prediction model. *Space Weather* **13**, 104. DOI.

Kaiser, M.L.: 2005, The STEREO mission: an overview. *Adv. Space Res.* **36**, 1483. DOI.

Kilpua, E.K.J., Balogh, A., von Steiger, R., Liu, Y.D.: 2017, Geoeffective properties of solar transients and stream interaction regions. *Space Sci. Rev.* **212**, 1271. DOI.

King, J.H., Papitashvili, N.E.: 2005, Solar wind spatial scales in and comparisons of hourly wind and ACE plasma and magnetic field data. *J. Geophys. Res.* **110**, A02104. DOI.

Kohutova, P., Bocquet, F.-X., Henley, E.M., Owens, M.J.: 2016, Improving solar wind persistence forecasts: removing transient space weather events, and using observations away from the Sun–Earth line. *Space Weather* **14**, 802. DOI.

Krivova, N.A., Balmaceda, L., Solanki, S.K.: 2007, Reconstruction of solar total irradiance since 1700 from the surface magnetic flux. *Astron. Astrophys.* **467**, 335. DOI.

Laker, R., Horbury, T.S., Bale, S.D., Matteini, L., Woolley, T., Woodham, L.D., Stawarz, J.E., Davies, E.E., Eastwood, J.P., Owens, M.J., O'Brien, H., Evans, V., Angelini, V., Richter, I., Heyner, D., Owen, C.J., Louarn, P., Fedorov, A.: 2021, Multi-spacecraft study of the solar wind at solar minimum: dependence on latitude and transient outflows. *Astron. Astrophys.* **652**, 105. DOI. Publisher: EDP Sciences.

Lang, M., Owens, M.J.: 2019, A variational approach to data assimilation in the solar wind. *Space Weather* **17**, 59. DOI.

Lang, M., Browne, P., van Leeuwen, P.J., Owens, M.: 2017, Data assimilation in the solar wind: challenges and first results. *Space Weather* **15**, 1490. DOI.

Lang, M., Witherington, J., Turner, H., Owens, M.J., Riley, P.: 2021, Improving solar wind forecasting using data assimilation. *Space Weather* **19**, e2020SW002698. DOI.

Langland, R.H., Baker, N.L.: 2004, Estimation of observation impact using the NRL atmospheric variational data assimilation adjoint system. *Tellus, Ser. A Dyn. Meteorol. Oceanogr.* **56**, 189. DOI.

Linker, J., Mikic, Z., Biesecker, D.A., Forsyth, R.J., Gibson, W.E., Lazarus, A.J., Lecinski, A., Riley, P., Szabo, A., Thompson, B.J.: 1999, Magnetohydrodynamic modeling of the solar corona during whole sun month. *J. Geophys. Res.* **104**, 9809. DOI.

Linker, J.A., Caplan, R.M., Downs, C., Riley, P., Mikic, Z., Lionello, R., Henney, C.J., Arge, C.N., Liu, Y., Derosa, M.L., Yeates, A., Owens, M.J.: 2017, The open flux problem. *Astrophys. J.* **848**, 70. DOI.

Linker, J.A., Heinemann, S.G., Temmer, M., Owens, M.J., Caplan, R.M., Arge, C.N., Asvestari, E., Delouille, V., Downs, C., Hofmeister, S.J., Jebaraj, I.C., Madjarska, M.S., Pinto, R.F., Pomoell, J., Samara, E., Scolini, C., Vršnak, B.: 2021, Coronal hole detection and open magnetic flux. *Astrophys. J.* **918**, 21. DOI. Publisher: American Astronomical Society.

Lockwood, M., Stamper, R., Wild, M.N.: 1999, A doubling of the Sun's coronal magnetic field during the past 100 years. *Nature* **399**, 437. DOI.

Low, B.C.: 2001, Coronal mass ejections, magnetic flux ropes, and solar magnetism. *J. Geophys. Res.* **106**, 25141. DOI.

Luhmann, J.G., Gosling, J.T., Hoeksmam, J.T., Zhao, X.: 1998, The relationship between large-scale magnetic field evolution and coronal mass ejections. *J. Geophys. Res.* **103**, 6585. DOI.

Luhmann, J.G., Larson, D., Hoeksema, J.T., Zhao, X.-P., Arge, N., St. Cyr, O.C.: 1999, Connections between the slow solar wind, CMES, and the helmet streamer belt inferred from coronal field models. *AIP Conf. Proc.* **471**, 725. DOI.

Luhmann, J.G., Ledvina, S.a., Odstrcil, D., Owens, M.J., Zhao, X.-P., Liu, Y., Riley, P.: 2010, Cone model-based SEP event calculations for applications to multipoint observations. *Adv. Space Res.* **46**, 1. DOI.

Mackay, D.H., Yeates, A.R.: 2012, The Sun's global photospheric and coronal magnetic fields: observations and models. *Living Rev. Solar Phys.* **9**, 6. DOI.

Manoharan, P.K.: 2012, Three-dimensional evolution of solar wind during solar cycles 22 – 24. *Astrophys. J.* **751**, 128. DOI.

McComas, D.J., Elliott, H.A., Schwadron, N.A., Gosling, J.T., Skoug, R.M., Goldstein, B.E.: 2003, The three-dimensional solar wind around solar maximum. *Geophys. Res. Lett.* **30**, 1517. DOI.

Merkin, V.G., Lyon, J.G., Lario, D., Arge, C.N., Henney, C.J.: 2016, Time-dependent magnetohydrodynamic simulations of the inner heliosphere. *J. Geophys. Res.* **121**, 2866. DOI.

Mursula, K., Hiltula, T.: 2003, Bashful ballerina: southward shifted heliospheric current sheet. *Geophys. Res. Lett.* **30**, 2135. DOI.

Narechania, N.M., Nikolić, L., Freret, L., Sterck, H.D., Groth, C.P.T.: 2021, An integrated data-driven solar wind – CME numerical framework for space weather forecasting. *J. Space Weather Space Clim.* **11**, 8. DOI. Publisher: EDP Sciences.

Odstrcil, D.: 2003, Modeling 3-D solar wind structures. *Adv. Space Res.* **32**, 497. DOI.

Odstrcil, D., Riley, P., Zhao, X.-P.: 2004, Numerical simulation of the 12 May 1997 interplanetary CME event. *J. Geophys. Res.* **109**, A02116. DOI.

Owens, M.: 2020, Solar-wind structure. In: *Oxford Research Encyclopedia of Physics*. DOI.

Owens, M.J., Crooker, N.U.: 2006, Coronal mass ejections and magnetic flux buildup in the heliosphere. *J. Geophys. Res.* **111**, A10104. DOI.

Owens, M.J., Forsyth, R.J.: 2013, The heliospheric magnetic field. *Living Rev. Solar Phys.* **10**, 5. DOI.

Owens, M.J., Lockwood, M.: 2012, Cyclic loss of open solar flux since 1868: the link to heliospheric current sheet tilt and implications for the Maunder Minimum. *J. Geophys. Res.* **117**, A04102. DOI.

Owens, M.J., Lockwood, M., Riley, P.: 2017, Global solar wind variations over the last four centuries. *Sci. Rep.* **7**, 41548. DOI.

Owens, M.J., Schwadron, N.A., Crooker, N.U., Hughes, W.J., Spence, H.E.: 2007, Role of coronal mass ejections in the heliospheric Hale cycle. *Geophys. Res. Lett.* **34**, L06104. DOI.

Owens, M.J., Challen, R., Methven, J., Henley, E., Jackson, D.R.: 2013, A 27 day persistence model of near-Earth solar wind conditions: a long lead-time forecast and a benchmark for dynamical models. *Space Weather* **11**, 225. DOI.

Owens, M.J., Riley, P., Lang, M., Lockwood, M.: 2019, Near-Earth solar wind forecasting using corotation from L5: the error introduced by heliographic latitude offset. *Space Weather* **17**, 1105. DOI.

Owens, M.J., Lang, M., Riley, P., Lockwood, M., Lawless, A.S.: 2020, Quantifying the latitudinal representivity of in situ solar wind observations. *J. Space Weather Space Clim.* **10**, 8. DOI.

Pizzo, V.: 1978, A three-dimensional model of corotating streams in the solar wind, 1. Theoretical foundations. *J. Geophys. Res.* **83**, 5563. DOI.

Press, W.H., Flannery, B.P., Teukolsky, S.A., Vetterling, W.T.: 1989, *Numerical Recipes*, Cambridge University Press, New York.

Richardson, I.G., Cane, H.V.: 2010, Near-Earth interplanetary coronal mass ejections during solar cycle 23 (1996 – 2009): catalog and summary of properties. *Solar Phys.* **264**, 189. DOI.

Richardson, I.G., Cane, H.V., Cliver, E.W.: 2002, Sources of geomagnetic activity during nearly three solar cycles (1972 – 2000). *J. Geophys. Res.* **107**, 1187. DOI.

Riley, P., Linker, J.A., Arge, C.N.: 2015, On the role played by magnetic expansion factor in the prediction of solar wind speed. *Space Weather* **13**, 154. DOI.

Riley, P., Linker, J.A., Mikic, Z.: 2001, An empirically-driven global MHD model of the solar corona and inner heliosphere. *J. Geophys. Res.* **106**, 15889. DOI.

Riley, P., Linker, J.A., Mikic, Z., Lionello, R., Ledvina, S.A., Luhmann, J.G.: 2006, A comparison between global solar magnetohydrodynamic and potential field source surface model results. *Astrophys. J.* **653**, 1510. DOI.

Riley, P., Linker, J.A., Lionello, R., Mikic, Z.: 2012, Corotating interaction regions during the recent solar minimum: the power and limitations of global MHD modeling. *J. Atmos. Solar-Terr. Phys.* **83**, 1. DOI.

Schatten, K.H., Wilcox, J.M., Ness, N.F.: 1969, A model of interplanetary and coronal magnetic fields. *Solar Phys.* **9**, 442. DOI.

Scherrer, P.H., Schou, J., Bush, R.I., Kosovichev, A.G., Bogart, R.S., Hoeksema, J.T., Liu, Y., Duvall, T.L., Zhao, J., Title, A.M., Schrijver, C.J., Tarbell, T.D., Tomczyk, S.: 2012, The Helioseismic and Magnetic Imager (HMI) investigation for the Solar Dynamics Observatory (SDO). *Solar Phys.* **275**, 207. DOI.

Simunac, K.D.C., Kistler, L.M., Galvin, A.B., Popecki, M.A., Farrugia, C.J.: 2009, In situ observations from STEREO/PLASTIC: a test for L5 space weather monitors. *Ann. Geophys.* **27**, 3805. DOI.

Smith, E.J.: 1990, The heliospheric current sheet and modulation of Galactic cosmic rays. *J. Geophys. Res.* **95**, 18731. DOI.

Solanki, S.K., Schüssler, M., Fligge, M.: 2000, Evolution of the Sun's large-scale magnetic field since the Maunder minimum. *Nature* **408**, 445. DOI.

Thomas, S.R., Fazakerley, A., Wicks, R.T., Green, L.: 2018, Evaluating the skill of forecasts of the near-Earth solar wind using a space weather monitor at L5. *Space Weather* **16**, 814. DOI.

Torok, T., Downs, C., Linker, J.A., Lionello, R., Titov, V.S., Mikić, Z., Riley, P., Caplan, R.M., Wijaya, J.: 2018, Sun-to-Earth MHD simulation of the 2000 July 14 "Bastille Day" eruption. *Astrophys. J.* **856**, 75. DOI.

Toth, G., Sokolov, I.V., Gombosi, T.I., Chesney, D.R., Clauer, C.R., De Zeeuw, D.L., Hansen, K.C., Kane, K.J., Manchester, W.B., Oehmke, R.C., Powell, K.G., Ridley, A.J., Roussev, I.I., Stout, Q.F., Volberg, O., Wolf, R.A., Sazykin, S., Chan, A., Yu, B., Kóta, J.: 2005, Space weather modeling framework: a new tool for the space science community. *J. Geophys. Res.* **110**, A12226. DOI.

Turner, H., Owens, M., Lang, M., Gonzi, S.: 2021, The influence of spacecraft latitudinal offset on the accuracy of corotation forecasts. *Space Weather* **19**, e2021SW002802. DOI.

Verscharen, D., Klein, K.G., Maruca, B.A.: 2019, The multi-scale nature of the solar wind. *Living Rev. Solar Phys.* **16**, 5. DOI.

Viall, N.M., DeForest, C.E., Kepko, L.: 2021, Mesoscale structure in the solar wind. *Front. Astron. Space Sci.* **8**, 139. DOI.

Vrsnak, B., Gopalswamy, N.: 2002, Influence of aerodynamic drag on the motion of interplanetary ejecta. *J. Geophys. Res.* **107**, 1019. DOI.

Wallace, S., Arge, C.N., Pattichis, M., Hock-Mysliwiec, R.A., Henney, C.J.: 2019, Estimating total open heliospheric magnetic flux. *Solar Phys.* **294**, 19. DOI.

Wang, Y.-M., Sheeley, J.N.R.: 1990, Solar wind speed and coronal flux-tube expansion. *Astrophys. J.* **355**, 726. DOI.

Webb, D.F., Howard, T.A.: 2012, Coronal mass ejections: observations. *Living Rev. Solar Phys.* **9**, 3. DOI.

Wilcox, J.M., Ness, N.F.: 1965, Quasi-stationary corotating structure in the interplanetary medium. *J. Geophys. Res.* **70**, 5793. DOI.

Yalim, M.S., Pogorelov, N., Liu, Y.: 2017, A data-driven MHD model of the global solar corona within Multi-Scale Fluid-Kinetic Simulation Suite (MS-FLUKSS). *J. Phys. Conf. Ser.* **837**, 012015. DOI.

Yeates, A.R., Mackay, D.H.: 2009, Initiation of coronal mass ejections in a global evolution model. *Astrophys. J.* **699**, 1024. DOI.

Yeates, A.R., Mackay, D.H., van Ballegooijen, A.A., Constable, J.A.: 2010, A nonpotential model for the Sun's open magnetic flux. *J. Geophys. Res.* **115**, A09112. DOI.